In vivo observation and biophysical interpretation of time-dependent diffusion in human white matter

Els Fieremans[*], **Lauren M. Burcaw**, **Hong-Hsi Lee**, **Gregory Lemberskiy**, **Jelle Veraart**, and **Dmitry S. Novikov**

Bernard and Irene Schwartz Center for Biomedical Imaging, Department of Radiology, New York University School of Medicine, New York, NY 10016, USA

Abstract

The presence of micrometer-level restrictions leads to a decrease of diffusion coefficient with diffusion time. Here we investigate this effect in human white matter *in vivo*. We focus on a broad range of diffusion times, up to 600 ms, covering diffusion length scales up to about 30 microns. We perform stimulated echo diffusion tensor imaging on 5 healthy volunteers and observe a relatively weak time-dependence in diffusion transverse to major fiber tracts. Remarkably, we also find notable time-dependence in the longitudinal direction. Comparing models of diffusion in ordered, confined and disordered media, we argue that the time-dependence in both directions can arise due to *structural disorder*, such as axonal beads in the longitudinal direction, and the random packing geometry of fibers within a bundle in the transverse direction. These time-dependent effects extend beyond a simple picture of Gaussian compartments, and may lead to novel markers that are specific to neuronal fiber geometry at the micrometer scale.

Keywords

Diffusion MRI; diffusion tensor imaging; STEAM sequence; time-dependent diffusion; hindered diffusion; white matter

Introduction

The unique advantage of diffusion-weighted magnetic resonance imaging (dMRI) arises from the sensitivity of water diffusion to the micrometer-level structure of its surrounding environment. In biological tissues, restrictions such as cell walls provide the basis for contrast in dMRI, and particularly, in diffusion tensor imaging (DTI) (Basser, 1995; Beaulieu, 2002). This contrast holds the promise of probing neuronal tissue structure at the scales of about three orders of magnitude below the nominal clinical MRI resolution. From the physics standpoint, this involves quantifying the relevant *length scales*, such as the compartment (cell) size, or the cell packing correlation length.

---

[*]Corresponding author: Phone: +1 (212) 263-3344; els.fieremans@nyumc.org.

There are two physically distinct ways of being sensitive to the cellular length scale: by varying the diffusion wave vector q, or by varying the diffusion time t, as illustrated in Fig. 1 of (Burcaw et al., 2015). The q-method, based on Callaghan's "diffusion diffraction" effect (Callaghan et al., 1991), measures the diffusion signal (the propagator) in the narrow pulse limit as function of q, and the length scale (the fully restricted pore size) is given by the inverse of the characteristic q value for which the propagator experiences oscillations. Unfortunately, given ~ 1 μm-diameter axons and dendrites, the required q values are prohibitively large for *in vivo* human measurements.

Instead, here our aim is to derive the relevant length scale(s) in human white matter (WM) by varying t, and studying the time-dependence $D(t)$ of the diffusion coefficient (more generally, of the diffusion tensor eigenvalues). This formally amounts to a $q \rightarrow 0$ measurement as the diffusion coefficient is proportional to a derivative of the dMRI signal at $q = 0$, which thereby makes our approach clinically feasible. Since the diffusion coefficient in a given direction x is a measure of the mean squared displacement, i.e. $D(t) = \langle (x(t) - x(0))^2 \rangle / 2t$, the length scale probed by water molecules may be adjusted by varying t. With increasing t, water molecules encounter more hindrances and restrictions to their diffusion paths, such as cellular walls and myelin, and therefore the resultant measured diffusion coefficient will decrease (Mitra et al., 1992; Novikov et al., 2014).

While time-dependence of the diffusion coefficient in mammalian WM has been clearly demonstrated at short times (~ 1 ms) (discussed in more detail below), *in vivo* evidence for the time-dependence using pulse gradient spin echo (PGSE) methods over clinically feasible diffusion time ranges ($t > 20$ ms) has been inconsistent. *In vivo* studies of brain, such as healthy and ischemic feline brain tissue (van Gelderen et al., 1994) yielded no change in the mean diffusivity with respect to t for a wide range encompassing 20 – 2000 ms. Nor was time-dependence observed *in vivo* in the mean diffusivity of human genu at relatively short times ($t = 8 – 80$ ms) (Clark et al., 2001) or in the longitudinal or transverse diffusivity within the human corticospinal tract for even longer times ($t = 64 – 256$ ms) (Nilsson et al., 2009). On the other hand, time-dependent diffusion has been observed *in vivo* in the corpus callosum, corona radiata, and brainstem of human subjects at times ranging from 40 to 800 ms (Horsfield et al., 1994). Furthermore, *ex vivo* studies in frog sciatic nerve with diffusion times of 2 ms and 28 ms (Beaulieu and Allen, 1996), bovine optic nerve with diffusion times ranging from 8 to 30 ms (Stanisz et al., 1997), optic and sciatic nerves with diffusion times from 3.7 ms to 99.3 ms (Bar-Shir and Cohen, 2008), as well as bovine optic nerve and rat spinal cord and brain with diffusion times from 40 to 250 ms (Assaf and Cohen, 2000) have shown a clear dependence of $D(t)$ on time in longitudinal and/or transverse direction. More recently, Kunz *et al.* (Kunz et al., 2013) imaged the rat corpus callosum *in vivo* at t ranging from 9 to 24 ms and found time-dependent diffusion in both longitudinal and transverse directions.

Oscillating gradient spin echo (OGSE) diffusion-weighted sequences are able to probe shorter diffusion times compared to conventional PGSE, and have demonstrated time-dependent diffusion in the brain. An *in vivo* oscillating gradient study of the rat cortex (Does et al., 2003) at frequencies up to 500 Hz, which correspond to very short $t \gtrsim 1$ ms, shows a clear time-dependence in the mean diffusivity in both normal live and post-mortem globally

ischemic rat cortex. Later work using OGSE with corresponding effective diffusion times (1 – 5ms) also demonstrated time-dependence in *ex vivo* rat WM tracts (Xu et al., 2014). In humans, Baron et al. (Baron and Beaulieu, 2014) combined OGSE (25 and 50 Hz) and PGSE methods (t = 20 and 40 ms) for a total diffusion time range of 4 to 40 ms, and found eight major WM tracts and two deep grey matter areas to exhibit time-dependent diffusion. Furthermore, recent work using double PFG MR indirectly points at the possibly non-Gaussian (time-dependent) nature of diffusion in the extracellular space of WM with increasing diffusion times from 25 to 100 ms (Shemesh and Cohen, 2011).

Here we report the observation of time-dependent diffusion *in vivo* for relatively long diffusion times, t = 45 – 600 ms, on a standard clinical scanner using STimulated Echo Acquisition Mode (STEAM)-DTI, and discuss the biophysical origin of this phenomenon. STEAM-DTI measurements were performed on 5 healthy volunteers and were calibrated on a gel phantom over the whole time range. Pronounced time-dependence in the longitudinal diffusivity and less pronounced time-dependence in the transverse diffusivity was found in both anatomically based WM regions and in fractional anisotropy (FA) thresholded regions.

The biophysical origin of the observed time-dependence, as discussed below, reflects the non-Gaussian nature of diffusion in at least one tissue compartment (in either direction). In all cases, both longitudinal and transverse diffusivities approach a finite tortuosity limit (i.e. diffusion is not anomalous (Bouchaud and Georges, 1990)), with a slow transient part that is best described by a power-law behavior (Novikov et al., 2014, Burcaw et al., 2015). We argue that the origin of this behavior is likely due to randomly placed (short-range disordered) hindrances and restrictions to diffusion in both parallel and transverse directions. Interestingly, the biological sources of this short-range disorder may be qualitatively distinct: structural disorder along the axons such as, e.g., varicosities for diffusion in the longitudinal direction, and the random packing geometry of fibers within a bundle for diffusion in the transverse direction. This picture is corroborated by the estimated correlation length scales in the range of a few microns in both directions.

Methods

In vivo measurements

Diffusion measurements were performed on 5 healthy volunteers (4 males and 1 female) ranging in age from 25 to 41 years old, on a 3T Siemens Tim Trio (Erlangen, Germany) equipped with a 32-channel head coil and a maximum gradient strength of 40 mT/m during two one-hour scans utilizing the STEAM-DTI sequence as provided by the vendor (WIP 511E). One volunteer was unable to be present for scan 2. Each diffusion sequence acquired b = 0 (5 averages) and b = 500 s/mm² images along 20 diffusion directions, with an isotropic voxel size of (2.7 mm)³, and a field of view (FOV) of (221 mm)². A slab of 15 axial slices was aligned parallel to the anterior commissure (AC) – posterior commissure (PC) line and centered such that the entire corpus callosum would be imaged. Both scans were focused on varying the diffusion time, t = (interpulse duration) ranging from 45 to 400 ms (scan 1) and from 55 to 600 ms (scan 2), while keeping δ, the pulse duration of the diffusion gradients, and TE, the echo time, constant. The parameters in these two scans were the following: δ = 20 ms, TE = 100 ms, TR = 7000 ms for t between 45 and 400 ms, with TR

increasing to 10200 ms at $t = 600$ ms. A summary of the specific parameters for each scan session can be found in Table 1.

Our *in vivo* measurement was calibrated by performing the same measurements on a nickel-doped agarose gel phantom, made by dissolving 1.4% agarose and 9 g/L of sodium chloride in distilled water and adding 2 mM Nickel and 6 g/L sodium azide, as described in (Lavdas et al., 2013). The gel was kept in a small cylindrical jar of roughly 10 cm long with a diameter of 6.5 cm.

Parameter Map Construction

In order to reduce the effect of Gibbs ringing surrounding the ventricles (Veraart et al., 2015), Gaussian filtering was applied to the dMRI images with a full width half maximum of 1.25 voxels and a window size of 5×5 voxels. To avoid cerebrospinal fluid (CSF) signal contamination in WM neighboring the ventricles during smoothing, a CSF mask was constructed via FSL's automated segmentation tool, FAST (Zhang et al., 2001) and used to separate the CSF from the rest of the brain parenchyma. These two resultant images (CSF and brain parenchyma) were smoothed separately using the parameters described above, which amounted to reducing the smoothing window size when getting close to the border, and recombined post smoothing.

Eigenvalues were calculated from the diffusion tensors that were estimated via a weighted linear least squares (WLLS) routine. The weights were derived from the DTI estimation by the unweighted LLS estimator (Veraart et al., 2013) and a corrected full *b*-matrix which incorporated the effective gradient from the diffusion, imaging gradients, and radiofrequency (RF) pulse magnetization inversions (Lundell et al., 2014; Sigmund et al., 2013). For the $b = 0$ image, the actual *b*-value (obtained from the trace of the *b*-matrix) varied from 2 s/mm^2 for $= 45$ ms, up to 67 s/mm^2 for $= 500$ ms, while the diffusion gradients were adjusted for the $b = 500$ image such that the actual $b = 500$ s/mm^2 (Lundell et al., 2014).

Previous work (Veraart et al., 2013) has determined that the WLLS estimator is unbiased if the Rician distributed data has SNR > 2. SNR was estimated in the $b = 0$ image via the ratio of a region of interest (ROI) placed in the splenium to an ROI placed in the background noise and corrected for the Rician statistics. We found that SNR varied from 15 for our shortest time down to 6 for our longest diffusion time at $b = 0$. Since the observed longitudinal and transverse diffusivities did not exceed 2 μm^2/s, the SNR on the DW images is sufficiently high to avoid a Rician noise bias.

The output parameter maps include the eigenvalues of the diffusion tensor **D**, the $S_{b=0}$ image, and fractional anisotropy (FA). Given the strong anisotropy of diffusion in major fiber tracts, it is natural to define the longitudinal diffusivity

$$D_\parallel(t) = \lambda_1 \quad (1)$$

in terms of the principal eigenvalue λ_1 of the diffusion tensor (the DTI eigenvalues are sorted according to $\lambda_3 \quad \lambda_2 \quad \lambda_1$), and the transverse diffusivity

$$D_\perp(t)=(\lambda_2+\lambda_3)/2 \quad (2)$$

as the axially symmetric component of the diffusion tensor projected onto the plane transverse to its principal eigenvector (tract direction).

ROI Selection

To ensure a consistent ROI selection across all scans, the b=0 images for each scan were registered to the b=0 image at t = 55 ms from scan 1 via a 12 parameter affine model using the FSL linear image registration tool, FLIRT (Jenkinson et al., 2002; Jenkinson and Smith, 2001). The output transformation matrix was used to register all parameter maps for each subject. Two types of ROIs were then outlined to investigate the time-dependence in WM.

The first type of ROI explored the role of increasing fiber alignment in the time-dependent diffusion. We created a series of ROIs, each containing all WM voxels within the selected volume based on a minimum FA threshold ranging from 0.3 to 0.7. The FA values used to define the threshold area were obtained from the mean FA values averaged over all diffusion times from scans 1 and 2 for each subject. A selection of FA-thresholded ROIs for a single subject are shown in Figure 1, panels a to d.

Second, anatomical WM ROIs were selected from the Johns Hopkins University WM atlas (Mori, 2005). The previously linearly registered subject FA maps were registered to the FA standard map in FSL using the non-linear registration tool, FNIRT. The warp maps produced from this registration were inverted and applied to the WM atlas ROIs to inversely register them to the subject space. These six anatomical ROIs include the corpus callosum genu and splenium, anterior corona radiata (ACR), superior corona radiata (SCR), posterior corona radiata (PCR), and the posterior limb of the internal capsule (PLIC). Examples of anatomical WM ROIs for a single subject are shown in Figure 1, panels e to f.

Statistical analysis

Mean longitudinal and transverse diffusivity values, Equations (1) and (2) respectively, were calculated for all ROIs. These ROI values were further used to gauge the appropriateness of the biophysical models described below (Equations (3)–(9)). To assess the overall magnitude of the time-dependence, the $D(t)$ data was transformed to a linear scale with respect to $1/t$ or $1/\sqrt{t}$ as suggested by some models (Equations (3), (4), (6)), and the significance of the corresponding model fits was assessed by the Pearson correlation coefficient and P-values, both listed in Tables 2 and 3. (These P-values were not used for justifying the models (3), (4) and (6), but rather to simply distinguish the observed time-dependence from a possibility of a noisy time-independent outcome.) Bonferroni correction was applied, multiplying the P-values by 22, to correct for multiple comparisons due to multiple ROIs (11 in total) and the two different models for the time-dependent diffusion coefficient (involving ordered and disordered types of restrictions, as explained below).

For both the longitudinal and transverse diffusion, when the fit was found to be significant ($P < 0.05$), the two different model fits were then compared using the R^2 values since the

appropriate models (ordered/disordered restrictions, intra/extra-axonal) have the same number of independent parameters, or degrees of freedom (dof).

Theory

Our recent framework for revealing mesoscopic structural universality classes via diffusion (Burcaw et al., 2015; Novikov et al., 2014) shows that the disorder class of the structure, represented by the structural exponent p, together with its effective spatial dimensionality d, dictates the functional form of how $D(t)$ approaches its bulk diffusion coefficient, D_∞. The exponent p determines the qualitative long-distance behavior of the density correlation function $\Gamma(r)$ of the restrictions to diffusion, formally defined via the asymptotic behavior of the Fourier transform (power spectrum of the restrictions) $\Gamma(k) \sim k^p$ as $k \to 0$.

Practically, depending on p and d, the diffusion coefficient will have long time asymptotic behavior of the form $D(t) \sim D_\infty + \text{const}/t^\vartheta$, with the dynamical exponent $\vartheta = (p + d)/2$, as long as $\vartheta < 1$; $D(t) \sim D_\infty + \text{const} \cdot (\ln t)/t$ if $\vartheta = 1$; and $D(t) \sim D_\infty + \text{const}/t$ if $\vartheta > 1$ or if water molecules are fully confined in-between impermeable walls (Burcaw et al., 2015; Novikov et al., 2014).

In either longitudinal ($d = 1$) or transverse direction ($d = 2$), the time-dependence of the overall $D(t)$ will be qualitatively different depending on whether the structural disorder is playing a role or not. In each case, we contrast the most common class of short-range disordered restrictions ($p = 0$) (whose effect was not considered in WM previously), with (pseudo-) ordered arrangements characterized by reduced long-range fluctuations ($p > 0$), or with the fully confining arrangements. We will then use the measured time-dependence and the estimated model parameters in both directions to identify whether the disorder is relevant, and based on that, suggest the biophysical interpretation of our observations.

Diffusion along the fiber tract, d = 1: Order or disorder?

Had the diffusion along axons been completely uniform along the tract, such as aligned hollow tubes, $D_\parallel$ would be constant. Time-dependence of $D_\parallel$ then should arise due to the structural "imperfections", or the deviations from the picture of hollow straight tubes. Indeed, the presence of varicosities or beads, resulting in varying axon diameters along their length (Perge et al., 2009; Shepherd and Raastad, 2003; Shepherd et al., 2002; Wang et al., 2003), or wave-like undulations (Nilsson et al., 2012), should hinder both intra- and extra-axonal diffusion (Budde and Frank, 2010). Other possible obstacles, such as mitochondria and oligodendrocytes, could also slow down the diffusion in the intra- and extra-axonal spaces, respectively.

If restrictions along the axonal direction are *periodic* ($p = \infty$), it follows from Equations (5) and (S25) in (Novikov et al., 2014), that $D_\parallel(t)$ will approach its long time limit D_∞ as

$$D_\parallel(t) \simeq D_\infty + \frac{c_1}{t}, \quad c_1 \sim a^2, \quad t \gg \frac{a^2}{D_0}, \quad (3)$$

where a is the period and D_0 is the free axoplasmic diffusion coefficient. More generally, the behavior (3) will also apply for any *hyperuniform* disorder with sufficiently strongly suppressed long-range fluctuations ($p > 1$), with a then corresponding to average spacing between the restrictions. In addition, any fully restricting domains along the axons of size $\sim a$ would also contribute as $\sim a^2/t$ to $D_\parallel(t)$ Hence, identifying the $\sim 1/t$ behavior in $D_\parallel(t)$ would prove that restrictions along the fibers are sufficiently strongly correlated (ordered) and/or fully confining (impermeable).

The histological evidence, however, typically points at a *short-range disorder*, characterized by a finite *correlation length* l_c. Physically, the correlation length reflects the distance from a given restriction, after which the "memory" about the positions of other restrictions disappears; formally, it gives the scale on which the correlation function $\Gamma(r)$ decays with r (in any spatial dimension d). For the $d = 1$ example of axonal beads (varicosities), the variance in their number within a window has been found to grow in proportion to the length of the window (Shepherd et al., 2002), which is a signature of a finite correlation length $l_c^\parallel$, in accord with the central limit theorem.

The short-range disorder would correspond to the structural exponent $p = 0$. In this case, from Equations (4) and (9) in (Novikov et al., 2014), $D_\parallel(t)$ will behave as

$$D_\parallel(t) \simeq D_\infty + \frac{c_2}{\sqrt{t}}, \quad c_2 = \frac{\Gamma_D(k \to 0)}{D_\infty} \frac{1}{\sqrt{\pi D_\infty}} \quad (4)$$

where $\Gamma_D(k \to 0) \approx D_\infty^2 l_c^\parallel$ is the $k \to 0$ limit of the Fourier transform of the two-point correlation function of the spatially varying coarse-grained diffusivity $D(x)$ (see Appendix A). It should be noted that while the power-law tail $1/\sqrt{t}$ in Equation (4) is scale invariant, its prefactor c_2 is sensitive to the disorder correlation length $l_c^\parallel$. Precise determination of this length scale depends somewhat on the shape of the restrictions, therefore the above relation between the correlation function limit $\Gamma_D(k \to 0)$ and $l_c^\parallel$ is approximate, but is still useful for making estimates; see Appendix A for more details about assumptions and practical limits. Note also that Equation (4) is equivalent to $\mathscr{D}(\omega) \approx D_\infty + \text{const} \cdot \sqrt{\omega}$ measured in cortical rat brain gray matter (Does et al., 2003; Novikov et al., 2014).

From the above constant, c_2, we estimate the disorder correlation length as

$$l_c^\parallel \approx c_2 \sqrt{\frac{\pi}{D_\infty}}. \quad (5)$$

A more in-depth discussion of our estimation of $l_c^\parallel$ can be found in Appendix A. Provided the diffusion time $t \gg \delta$, as in our case, the asymptotic inverse square root behavior (4) of $D_\parallel(t)$ should qualitatively hold irrespective of the influence of finite-width diffusion gradient pulses (Lee et al., 2015).

Diffusion transverse to the fiber tract, d = 2: Intra- or extra-axonal?

The time-dependence of diffusion transverse to a WM tract has been previously considered as arising solely from the intra-axonal compartment, while diffusion in the extra-axonal compartment has been assumed Gaussian (Alexander et al., 2010; Assaf et al., 2008; Assaf et al., 2004; Barazany et al., 2009; Zhang et al., 2011). Recently, we suggested that the extra-axonal contribution to the overall $D_\perp(t)$ dominates (Burcaw et al., 2015) due to the disordered packing geometry of axons. Here we compare the two pictures: the conventional "intra-axonal" one (with Gaussian extra-axonal diffusion), and the "extra-axonal" picture where for simplicity we assign all time-dependence to the extra-axonal space while the intra-axonal contribution to the overall diffusion signal attenuation is neglected in comparison.

In the intra-axonal picture, the intra-axonal space is treated as that within impermeable cylinders. The exact signal attenuation to the lowest order, G^2, in the applied diffusion gradient G is found by (Murday and Cotts, 1968; van Gelderen et al., 1994). For studying the functional dependence with respect to t and δ, here we consider the two simpler limits: the narrow pulse limit $\delta \ll \tau_D$ and the wide pulse, or the Neuman's limit $\delta \gg \tau_D$, where $\tau_D = r^2/D_0$ is the characteristic time to diffuse across an axon with radius r.

In the narrow pulse limit, the intra-axonal contribution to $D_\perp(t)$ decreases as $r^2/(4t)$, which follows from the exact result (Callaghan and Stepišnik, 1995; Stepišnik, 1993) for $t \gg \delta_D$ (this condition practically always holds for our very long times t). When averaged over a voxel during measurement, the overall $D_\perp(t)$ is a weighted average (Burcaw et al., 2015),

$$D_\perp(t)|_{\delta \ll \tau_D} \simeq f_{\text{int}} \cdot \frac{r^2}{4t} + f_{\text{ext}} D_\infty^{\text{ext}}, \quad f_{\text{int}} + f_{\text{ext}} = 1, \quad (6)$$

where f_{int} and f_{ext} are the intra- and extra-axonal water fractions, and r becomes a typical inner axonal radius such that $r^2 \equiv \langle r^4 \rangle / \langle r^2 \rangle$. The term $f_{\text{ext}} D_\infty^{\text{ext}}$ in Equation (6) comes from the Gaussian diffusion assumption for the extra-axonal space.

In the opposite, wide pulse limit $\delta \gg \tau_D$, the intra-axonal contribution to the overall signal attenuation is described by Neuman's formula (Neuman, 1974), $-\ln \frac{S_{\text{int}}}{S_0} \simeq \frac{7}{48} \frac{(\gamma G)^2 r^4 \delta}{D_0}$. Therefore, the overall diffusion coefficient, defined via $-\ln S/S_0 = bD_\perp(t) + O(b^2)$, where $b = (\gamma G \delta)^2 \left(t - \frac{\delta}{3} \right)$, is a weighted average

$$D_\perp(t, \delta)|_{\delta \gg \tau_D} \simeq \frac{7}{48} \frac{f_{\text{int}} r^4}{D_0} \frac{1}{\delta \left(t - \frac{\delta}{3} \right)} + f_{\text{ext}} D_\infty^{\text{ext}}, \quad t \geq \delta. \quad (7)$$

Unfortunately, the measured diffusion coefficient does not allow us to determine f_{int} and f_{ext} separately (for that, one would need to measure higher-order diffusion cumulants). Hence, if the conventional intra-axonal picture is correct, at the DTI level we can only determine the combination $r \sqrt{f_{\text{int}}}$ for the narrow pulse limit, Equation (6), or the combination $r(f_{\text{int}}/D_0)^{1/4}$ for the case of wide pulses, Equation (7), where now $r^4 \equiv \langle r^6 \rangle / \langle r^2 \rangle$ after averaging over the voxel. Setting $f_{\text{int}} \to 1$, we can obtain the *lower bound* on typical axonal diameters $2r$ in

either limit, assuming the diffusion time-dependence arises solely from the intra-axonal compartment.

In the extra-axonal picture, extra-axonal contribution to the overall $D_\perp(t, \delta)$ is nontrivial and dominates. Here, we will also distinguish between narrow and wide pulse limits. Instead of the intra-axonal diffusion time τ_D, the relevant time scale to be compared with the pulse width δ is the correlation time t_c. This is the time to diffuse across the correlation length $l_c^\perp \simeq \sqrt{2dD_\infty t_c}$, $d = 2$, of the axonal fiber packing in the tract cross-section.

Assuming short-range disorder ($p = 0$) in the axonal placement within a fiber bundle cross-section, the extra-axonal contribution to the overall transverse diffusion coefficient should follow a logarithmically enhanced time-dependence (Burcaw et al., 2015):

$$D_\perp(t) \simeq f_{\text{ext}}D_\infty^{\text{ext}} + f_{\text{ext}}A \cdot \tfrac{\ln(t/\tilde{t}_c)}{t}, \quad t \gg \tilde{t}_c \sim \max\{t_c, \delta\}, \quad (8)$$

where the coefficient A is proportional to the limit $\Gamma(k{\to}0)$ of the power spectrum $\Gamma(k)$ of the axonal fiber density in cross-section (Burcaw et al., 2015; Novikov et al., 2014).

In Equation (8) we neglected the $\sim 1/t$ intra-axonal contribution (cf. Equations (6) and (7) above) since it decays faster with t than the extra-axonal $(\ln t)/t$ term. Effectively, the neglected contribution could modify the parameter $\tilde{t}_c$ under the logarithm during fitting. Fitting simultaneously intra- and extra-axonal contributions is quite challenging, since fitting to smoothly decaying curves becomes unstable with an increase in the number of degrees of freedom, and it is especially difficult to obtain robust estimates for parameters under the logarithm. We also note that, depending on the relation between δ and t_c (the latter *a priori* unknown), Equation (8) has either 2 or 3 degrees of freedom.

In the narrow pulse limit $\delta \ll t_c$, the result (8) is independent on the pulse width, dof = 3, and $l_c^\perp$ can be estimated from t_c as pointed above. However, in the wide pulse limit $\delta \gtrsim t_c$, the diffusion measurement acts as a low-pass filter, the result becomes insensitive to the correlation time, dof = 2, and $D_\perp(t)$ instead follows (Burcaw et al., 2015)

$$D_\perp(t, \delta) = f_{\text{ext}}D_\infty^{\text{ext}} + f_{\text{ext}} \cdot \tfrac{A}{2\delta^2(t-\frac{\delta}{3})}\left[t^2\ln\tfrac{t^2-\delta^2}{t^2} + \delta^2\ln\tfrac{t^2-\delta^2}{\delta^2} + 2t\delta\ln\tfrac{t+\delta}{t-\delta}\right], \quad (9)$$

where $t = $ is the inter-pulse duration. The second term of Equation (9) has an asymptotic $f_{\text{ext}}A \ln(t/\delta)/t$ behavior for $t \gg \delta$, cf. Equation (8). Thus, if an actual $t_c \lesssim \delta$, we would practically determine δ instead of t_c using Equation (8), and the intrinsic value of t_c will be "washed out" by the wide pulses. In this case, the correlation length $l_c^\perp$ can only be determined from the amplitude A of the transient contribution, similar to the longitudinal case, cf. Equations (4) and (5). In (Burcaw et al., 2015), we empirically estimated

$$A \approx 0.2\, l_c^{\perp^2}. \quad (10)$$

The scaling of A with $l_c^{\perp 2}$ is justified by the dimensional considerations (see Appendix A of (Burcaw et al., 2015), similar to the longitudinal case above), and the numerical coefficient 0.2 is an empirical number depending on the random packing geometry used in our numerical simulations. This coefficient might have a somewhat different value for axons packed *in vivo*; unfortunately, there is no way to know their precise packing geometry at present. So, much like the factor $\sqrt{\pi}$ in Equation (5), the coefficient 0.2 in Equation (10) is approximate, reflecting a non-universal dependence of the correlation length on the correlation function limit $\Gamma_D(k \to 0)$.

As we do not *a priori* know how t_c relates to δ, our strategy in the transverse case is to first use Equation (8) in order to determine $\tilde{t_c}$. Then, depending on its value, we either identify $t_c = \tilde{t_c}$ if $\tilde{t_c} > \delta$ which would justify *a posteriori* the use of Equation (8) with dof = 3; or, in the opposite case $\tilde{t_c} \lesssim \delta$, we will have to revert to Equation (9) with dof = 2, and rely on the less accurate relation (10) in order to estimate $l_c^{\perp}$ from the transient amplitude A. Since f_{ext} is unknown, and it is only the combination $f_{ext} A$ that can be determined from a fit, we can estimate the combination $l_c^{\perp} \sqrt{f_{ext}}$ that practically sets the *lower bound* on $l_c^{\perp}$.

Results

We ran the scan 1 and 2 STEAM protocols on a gel phantom and the resulting diffusivities with respect to time are shown in Figure 2, demonstrating no substantial change with time. The values for T_1 and T_2 of the phantom were measured to be 364.3 ±34 ms and 63.6 ± 5.6 ms, respectively.

Results from the anatomical WM ROIs for scans 1 and 2 show time-dependence in the *longitudinal diffusivity* $D_{\parallel}(t)$ as seen in Figure 3 for all WM ROIs investigated. The overall decrease in $D_{\parallel}(t)$ in all ROIs is also supported by significant *P*-values in Table 2 for either model. For ROIs outside the corpus callosum, the *transverse diffusivity* $D_{\perp}(t)$ also exhibits time-dependence. While the decrease is less pronounced, it is still significant in the WM ROIs outside the corpus callosum (as supported by the significant *P*-values in Table 3).

Results for the ROIs based on FA thresholding are presented in Figure 4, which shows $D_{\parallel}(t)$ and $D_{\perp}(t)$ averaged over all subjects and over both scans 1 and 2. Overall we see a slight decrease with time for $D_{\perp}(t)$ and a more pronounced decrease in $D_{\parallel}(t)$ in absolute terms, however the relative change for $D_{\perp}(t)$ is greater than that for $D_{\parallel}(t)$ as evidenced by the percentage change in Tables 2 and 3. As the FA threshold is increased, $D_{\parallel}(t)$ becomes more strongly time dependent, while $D_{\perp}(t)$ decreases overall and its time-dependence becomes weaker. Similarly to the results for the anatomical WM ROIs, $D_{\parallel}(t)$ decreases significantly with time for all FA thresholded ROIs. On the other hand, $D_{\perp}(t)$ shows observable time-dependence for FA 0.5, but this dependence is not pronounced in those voxels selected based on a higher FA threshold, that correspond mostly to voxels in the corpus callosum. This observation agrees with the anatomical WM results of the genu and splenium of the corpus callosum that also do not exhibit clear time-dependence in the transverse direction.

Model Selection and Parameter Estimation

Longitudinal diffusion—For both the anatomical WM ROIs and FA thresholded ROIs, $D_\parallel(t)$ from scans 1 and 2 averaged over all subjects for each diffusion time are plotted in Figure 5 along with the fit (dashed lines) of Equations (3) and (4). Corresponding fit parameters are shown in Table 2. Assuming ordered (or hyperuniform) restrictions, Equation (3) results in a mean spacing of restrictions $a \sim 3\text{–}5$ μm for both WM and FA ROIs. On the other hand, assuming short-range disordered restrictions, Equation (4) results in correlation length values on the order of $l_c^\parallel \sim 3\text{–}7$ μm.

For all regions in both the anatomical WM and FA thresholded ROIs, the fit to short-range disorder model (4) results in higher R^2 values, indicating a higher fit quality (with the same number of degrees of freedom). Besides, the curves become closer to straight lines when plotted as function of $t^{-1/2}$ than t^{-1}. This finding agrees with histology evidence of short-range disorder along axons, as discussed in more detail below.

Transverse diffusion—Figure 6 shows models of $D_\perp(t)$, for either intra-axonal or extra-axonal picture, fit to the transverse diffusivities averaged over both anatomical WM and FA thresholded ROIs. The left column shows the fits assuming time-dependence due to intra-axonal diffusion, either in the narrow pulse limit (dashed line, Equation (6)) or for wide pulse limit (solid line, Equation (7)). The fits for the narrow and wide pulse limits are similar and in fact are hard to distinguish. This is not surprising, since for $t \gg \delta$ both Equations (6) and (7) yield the same functional dependence on t.

The right column shows the fits assuming time-dependence due to extra-axonal diffusion through a disordered 2-dimensional packing geometry, either in the narrow pulse limit (dashed line, Equation (8)), or for finite pulse width (solid line, Equation (9)). For both the anatomical WM and FA thresholded ROI data, the resultant fit parameters for Equations (6)–(7), and (8)–(9), are shown in Table 3.

In the case of extra-axonal diffusion determining the time-dependence, cf. Equation (8), the estimated values for $\tilde{t}_c$ appear fairly close to the pulse width δ set to 20 ms. Therefore, if the disordered picture is correct, it is more appropriate to use Equation (9) to determine tissue parameters, i.e. we are here in the "wide-pulse" limit which washes out the correlation time under the logarithm. The corresponding fit values of $f_{ext} A$ and $D_\infty = f_{ext} D_\infty^{ext}$ based on Equation (9) are presented in Table 3. We then use Equation (10) to estimate $l_c^\perp \sqrt{f_{ext}}$ that sets the lower bound on the transverse correlation length $l_c^\perp$.

Having selected the wide-pulse limit (9) for the extra-axonal picture, we now can compare it with the fits for intra-axonal models (Equations (6) and (7)). While all these equations appear to fit the data with respect to t well, when the data is replotted with respect to t^{-1}, Equations (6) and (7) fail to fully capture the systematic non-linear *downward bending (concavity)* in the time-dependence of $D_\perp(t)$ (Figure 6c–d, g–h). We can also compare the R^2-values of Equations (6), (7) and (9) since they all have the same dof = 2, which shows that the R^2-values for model (9) are consistently higher. We can interpret this increased fit

quality in terms of taking into account the systematic $\sim \ln t$ deviations from the $1/t$ behavior presumably occurring due to the short-range disorder in the extra-axonal space.

We discuss and contrast the apparent values of axonal diameters and of the disorder correlation lengths in the following Section.

Discussion

With this study, we aimed to measure time-dependent diffusion in WM *in vivo* using clinical PGSE MR methods, and to provide a plausible interpretation of this effect in terms of the cellular length scales. Our results show that for both anatomical and FA-thresholded WM ROIs, a pronounced longitudinal time-dependence and a weaker (in absolute terms) transverse time-dependence of the diffusion coefficient are observed for the 45 – 600 ms diffusion times measured here using a STEAM sequence in 5 healthy volunteers.

The main benefit of the STEAM sequence is the elimination of T_2 relaxation effects during the mixing time TM, that allows us to go to relatively long diffusion times without losing signal from T_2 dephasing. Additionally, the elimination of T_2 effects in the STEAM sequence will alleviate the possible effect of unequal T_2 pools (Szafer et al., 1995). By fixing TE and δ, we strive to eliminate any effect which varying these parameters may have, such as surface relaxation or dephasing via exchange with myelin.

Below, we first list potential confounding effects, and subsequently provide arguments why the observed time-dependence could at least in part be an effect of diffusion gradually slowed down due to the microstructural environment. Next, we provide a biophysical interpretation of both the observed longitudinal and transverse time-dependence and discuss the estimated correlation length scales as obtained from the appropriate tissue models that include effects of randomly placed restrictions on the amplitude of the power-law contributions to $D(t)$.

Potential confounding effects

SNR decrease with increasing mixing time due to the T₁ relaxation—To derive the diffusion coefficient from the diffusion weighted signals, we normalize them by the b=0-signal with the same STEAM preparation. This eliminates contamination by the T_1-weighted signal decrease with the mixing time TM under the assumption of monoexponential T_1 relaxation (Merboldt et al., 1985; Tanner, 1970). Our measurements on an isotropic gel phantom with similar T_1 and T_2 relaxation times as observed *in vivo*, also confirmed no demonstrable effect of T_1 relaxation on the diffusion coefficient for increasing TM. Furthermore, as reported above, we have an SNR > 2 for = 600 ms which exceeds the required SNR threshold to allow for unbiased estimation of the diffusion tensor from Rician distributed data in logarithmic space (Salvador et al., 2005).

Multiple T₁ components—These can correspond to intra- and extra-axonal spaces (both *NMR visible*), and to myelin water (*NMR invisible*, because of short myelin T_2). We consider these two cases separately. Furthermore, the physics depends on whether exchange is able to

occur on the time scale of our measurement (Fieremans et al., 2010; Stanisz, 2003; Szafer et al., 1995).

Different T_1 values for intra/extra axonal water (both compartments are NMR visible)—While multiple long T_1 components (850 and 2800 ms), respectively attributed to the intra-axonal space of myelinated axons, and to the mixture of extra-axonal space and intra-axonal space of non-myelinated axons, have been reported in (Lancaster et al., 2003), more evidence in literature can be found for a *single* long T_1 relaxation component, as measured in rat corpus callosum (Does and Gore, 2002), bovine corpus callosum (Bjarnason et al., 2005; Henkelman et al., 1994), and mouse WM (Stanisz et al., 2005). (Mulkern et al., 2000) specifically studied the effect of T_1 relaxation on the fast and slow component of ADC in human WM and found that the corresponding (long) T_1 components were not significantly different. Assuming similar T_1 values in both components and a fairly low exchange rate due to layers of myelin, the overall diffusivity is then given by the weighted average of the two pools (Fieremans et al., 2010), and therefore does *not* depend on time. In case of different T_1 in each compartment, the resulting ADC would depend on the mixing time through the exponentially varying compartment weights.

Effect of myelin water with short T_1 (exchange with an NMR invisible compartment)—Biexponential T_1 relaxation has been reported, with a *short* T_1 component of about $T_1^{\text{short}} \approx 50$ ms, originating, presumably, from water in-between myelin sheets (Does and Gore, 2002; Rioux et al., 2015). By itself, this compartment is NMR-invisible, since the relatively long TE of 100 ms in our experiment greatly exceeds myelin water T_2 value, measured around 10–20 ms (Does and Gore, 2002; Stanisz et al., 1999; Whittall et al., 1997).

However, exchange or surface relaxation with the "silent" myelin compartment can potentially affect the measured ADC, which no longer is given by the weighted average between myelin and free water diffusivities. A *single* exchange event will not contribute to the observed ADC, as the protons exchanged with myelin become invisible due to its short T_2. However, water molecules undergoing *multiple* exchange events (e.g. spending some time inside myelin and coming back), or equivalently, temporarily relaxing at the myelin surface, may still contribute to the diffusion signal if the exchange or surface relaxation happens during the *mixing period* when spins are aligned with the main magnetic field and therefore do not undergo T_2, but rather T_1 relaxation. As we vary TM, these exchanged or relaxed protons will contribute to the measured signal, weighted by different T_1's in each compartment. Assuming they diffuse more slowly inside myelin or when relaxing on the surface, this will also lead to a decrease of the ADC with TM. While modeling this effect is beyond the scope of this work, we note that this temporary residence inside myelin or myelin water would also have to slow down the diffusion in *both* longitudinal and the transverse directions, contrary to our observation that with increasing FA threshold (presumably equivalent to keeping voxels with more myelin), the longitudinal $D(t)$ becomes more pronounced while the transverse $D(t)$ becomes less pronounced (Figure 4).

Longitudinal Diffusion

The existence of longitudinal time-dependence suggests restrictions are present along the axons, making the commonly used "hollow tube" model for modeling diffusion inside and outside axons (Assaf et al., 2004; Behrens et al., 2003; Jespersen et al., 2007; Kroenke et al., 2004; Ong et al., 2008) incomplete as long as the longitudinal diffusion is not in the tortuosity limit. While both periodic and disordered models (with the same dof) fit the longitudinal data well, the fits of the disordered model demonstrate higher R^2 values for all ROIs examined, suggesting the longitudinal restrictions are more likely to be short-range-disordered rather than ordered or hyperuniform along fibers. It is of interest to note that a similar phenomenon has recently been invoked to explain the apparent $\sqrt{\omega}$ frequency dependence of previously measured OGSE diffusion in rat cortical grey matter (Does et al., 2003; Novikov et al., 2014). While there, the effectively one-dimensional diffusion has been occurring presumably mostly along the dendrites rather than axons, it may as well be that here we are observing a similar phenomenon from the diffusion physics standpoint and witnessing, at much longer times, what remains of the more pronounced $\sqrt{\omega} \sim 1/\sqrt{t}$ quasi-one-dimensional behavior seen with OGSE. It would be interesting to study how universal this time/frequency dependence due to short-range disorder is along neurites (axons and dendrites) *in vivo*.

Which anatomical features could restrict the diffusion along the axons over the observed time scale? Nodes of Ranvier are very low in density (typical internodal length is 300–400 μm (Perrot et al., 2007)), and are therefore not likely as significant source of restrictions. Intriguingly, the correlation length scales $l_c^{\parallel}$ are on the order of 3–6 μm which are similar to those reported in the literature for varicosities along axonal fibers (Debanne et al., 2011; Shepherd and Raastad, 2003; Shepherd et al., 2002; Wang et al., 2003), suggesting them as potential sources for the reduction in $D_{\parallel}(t)$ over time. Varicosities are found to be often rich in mitochondria and therefore could form obstacles for the diffusion along the fibers. The disordered geometry in the extra-axonal space due to varicosities would also slow down the extra-axonal contribution to $D_{\parallel}(t)$. It is natural to assume that the correlation lengths inside and outside axons would be similar, as the corresponding restrictions mirror each other. Other potential sources for the short range disorder could be axonal undulations (Nilsson et al., 2012), or the functional gap junctions, which are found to be unevenly spaced between 20 and 60 μm along the myelin sheath in sciatic nerve (Schain et al., 2014). At present, we cannot separate the intra- and extra-axonal contributions to the overall $D_{\parallel}(t)$; identifying which one is dominant, or whether they are similar, remains an exciting unresolved question.

Transverse Diffusion

In addition to the decrease of the longitudinal diffusion with time, a decrease in transverse diffusivity is also observed in WM regions outside the corpus callosum. What is the mesoscopic origin of the transverse time-dependence? In principle, one could speculate that the transverse time-dependence may just be that of the diffusion *along* the elementary fibers within a bundle, projected onto the plane transverse to the main fiber tract direction, if we assume some orientational fiber dispersion, as illustrated in Figure 7. As such effect could

potentially explain the weakening of the transverse time-dependence for increasing FA (Figure 4), we tried to estimate its contribution in Appendix B. Assuming an axially symmetric orientational dispersion of fiber segments at an angle θ to the overall fiber tract, we calculate segments' eigenvalues $\lambda_{\parallel}(t)$ and $\lambda_{\perp}(t)$ based on the overall observed diffusion tensor eigenvalues $D_{\parallel}(t)$ and $D_{\perp}(t)$ as functions of θ. We then determine the angle θ needed to eliminate the time-dependence in $\lambda_{\perp}(t)$ under the hypothesis that all the transverse time-dependence for the segments is artificial, and the observed voxel-wise $D_{\perp}(t)$ is caused by $\lambda_{\parallel}(t)$ combined with the orientational dispersion. We find that θ for all anatomical WM ROIs and FA thresholds is notably greater (Table B1) than reported values of axon dispersion of about 18° (Ronen et al., 2014) (for more details see Appendix B). Therefore we conclude that orientational fiber dispersion alone cannot explain the time-effect in the transverse diffusion, and the time dependent diffusion presumably has a significant "microstructural", or "mesoscopic" component, presumably due to the structural disorder, as outlined in the *Results* Section.

As the transverse $D(t)$ effect cannot be explained by the longitudinal $D(t)$ and orientational dispersion alone, the choice is then essentially between intra-axonal (confinement) and extra-axonal (structural disorder) pictures, Equations (6)–(7) versus Equation (9), respectively. Based on the fitting, the R^2 parameter selects the "disordered" extra-axonal model (9) in all anatomical and FA-based ROIs. To determine the more appropriate model, we should also consider the plausibility of the values of biophysical parameters resulting from both models.

The intra-axonal picture of Equations (6) and (7) sets *lower bounds* on the inner axonal diameters $2r$ in the range of 10–13 μm (when setting $f_{int} \to 1$, Table 3). With realistic values of water fraction f_{int} closer to 0.5 (this estimate is based on excluding myelin volume), the apparent axonal diameters $2r$ will be around at least 15 μm in either narrow-pulse limit (6) or Neuman's limit (7); for the latter one, we take $D_0 \gtrsim 2 \ \mu m^2/ms$ (Beaulieu, 2002). With the estimated $r \sim 7$ μm, the diffusion time across an axon $\tau_D \sim \delta$, which falls in-between the narrow-pulse and Neuman's limits (6) and (7); however, as the estimate for r is practically the same for both limits, the full van Gelderen's formula interpolating between them should provide the same estimate, which we checked using reasonable values for f_{int} and D_0. However, fitting the data directly with van Gelderen's formula was very imprecise since it has dof = 3.

The apparent axonal diameter values obtained in the intra-axonal picture are a factor of 10 greater than the inner diameter values $\lesssim 1$ μm reported in (Aboitiz et al., 1992) in the human corpus callosum; 99% of all axons there have diameters below 3 μm (Innocenti et al., 2015). We note that a similarly strong overestimation of axonal diameters has been previously reported based on the same physical picture as that employed to derive Equations (6) and (7) (Alexander et al., 2010). Outside the corpus callosum, axonal diameters are generally of the same order of ~1 μm. For instance, Tang et al. reported an average *outer* diameter for myelinated axons in the WM of one complete human brain hemisphere as 1.14 μm using stereology of light microscopy (Tang and Nyengaard, 1997), which would put average inner diameter well below 1 μm given typical myelin *g*-ratio of about 0.6 – 0.7. As a result, comparing the parameters of the models (6)–(7) and (9), we suggest that the interpretation of

time dependent diffusion as originating solely from the finite axonal diameter values is most likely insufficient, at least for human brain measurements. Our suggestion is also supported by recent *ex vivo* rat spinal cord measurements (Xu et al., 2014) that provided evidence in favor of incorporating the linear-in-frequency extra-axonal OGSE diffusivity dependence, a counterpart of Equations (8) and (9) in the time domain (Burcaw et al., 2015; Novikov et al., 2014).

The extra-axonal picture, on the other hand, yields the 2-dimensional disorder correlation length $l_c^\perp \approx 4-5\,\mu\text{m}$ (Table 3). This value is three-fold smaller than the inner diameter estimate from the intra-axonal picture, and approaches the *outer* axonal diameter values (including myelin). Also, local short-range order in the axonal packing could make $l_c^\perp$ notably exceed the typical outer diameter. Hence, this estimate for the relevant length scale seems more biologically plausible, and together with higher R^2 fit values, our parameter estimation results support the extra-axonal picture. Our findings are also in agreement with our recent modeling and phantom experiments (Burcaw et al., 2015), although our values of $l_c^\perp$ and A are notably larger than those determined from Monte Carlo simulations in that work. This could be due to using somewhat smaller monkey corpus callosum axon diameter values, as well as due to strong sensitivity of $l_c^\perp$ and A to the axonal packing geometry (cf. Fig. 4 of Burcaw et al., 2015) that is unknown *in vivo*.

Overall, we show here that the disordered packing geometry, essential for diffusion in the extra-axonal space, is more relevant in the overall time-dependence of the diffusion coefficient, thereby underscoring a higher sensitivity of the low-*b* DW signal to the extra-axonal arrangement than to the intra-axonal compartment size at clinically feasible diffusion times. This suggests a possible novel kind of contrast to the mesoscopic structural correlations and fiber packing geometry within axonal tracts.

Outlook and open questions

While the observed *t*-dependent effects are subtle, our results point at exciting non-Gaussian effects of mesoscopic structure of axonal fibers on diffusion, able to provide relevant tissue length scales corresponding to different physical origins in the parallel and in the transverse directions. The current protocol focused on relatively low diffusion weighting ($b = 0.5$ ms/μm^2) and long diffusion times (45 ms – 600 ms). Our results are suggesting to explore the crossover to shorter times, where the time dependence is likely to be more pronounced; to establish which compartment contributes most to the observed time-dependence, especially to the less explored one in the longitudinal direction (e.g. by increasing the diffusion weightings); as well as to quantify the relative importance of exchange with myelin. We also believe Monte Carlo simulations of diffusion in a realistic axonal geometry can shed light on the dependence of the mesoscopic parameter values, such as the disorder correlation length and the amplitude of the power-law tails, on the WM tract geometry. Finally, since the acquisition scheme is clinically feasible, we think it could be very interesting to evaluate the time-dependence and the derived structural parameters in clinical applications.

Conclusions

We report here a pronounced longitudinal time-dependence and a weaker (in absolute terms) transverse time-dependence of diffusion tensor eigenvalues in white matter regions observed between 45 ms and 600 ms on a clinical scanner using a STEAM sequence in five healthy volunteers. The observation of time-dependence in both longitudinal and transverse directions is interpreted as an effect of structural disorder at the mesoscopic scale, which is beyond the commonly used physical picture of Gaussian tissue compartments. It also highlights the non-Gaussian nature of diffusion in at least one of the compartments in the longitudinal direction, and unexpectedly, in the extra-axonal compartment in the transverse direction.

In particular, the longitudinal time-dependence suggests that the "hollow-tube" model of neurites (axons) is incomplete, and should be complemented by the disordered restrictions along the fibers, with the correlation length of a few micrometers. Furthermore, the radial time-dependence seems to be dominated by the extra-axonal water diffusion, due to the short range packing disorder of the axons within the bundle, rather than from the intra-axonal water diffusion. Overall, these mesoscopic effects, first reported here in an *in vivo* human diffusion MRI measurements on a clinical scanner, may enable a novel kind of structural contrast at the micrometer scale, and open up exciting possibilities of monitoring subtle changes of structural arrangements within neuronal tracts in disease, aging, and development.

Acknowledgments

References

Aboitiz F, Scheibel AB, Fisher RS, Zaidel E. Fiber composition of the human corpus callosum. Brain Research. 1992; 598:143–153. [PubMed: 1486477]

Alexander DC, Hubbard PL, Hall MG, Moore EA, Ptito M, Parker GJM, Dyrby TB. Orientationally invariant indices of axon diameter and density from diffusion MRI. Neuroimage. 2010; 52:1374–1389. [PubMed: 20580932]

Assaf Y, Blumenfeld-Katzir T, Yovel Y, Basser PJ. AxCaliber: A method for measuring axon diameter distribution from diffusion MRI. Magnetic Resonance In Medicine. 2008; 59:1347–1354. [PubMed: 18506799]

Assaf Y, Cohen Y. Assignment of the water slow-diffusing component in the central nervous system using q-space diffusion MRS: Implications for fiber tract imaging. Magnetic Resonance In Medicine. 2000; 43:191–199. [PubMed: 10680682]

Assaf Y, Freidlin RZ, Rohde GK, Basser PJ. New modeling and experimental framework to characterize hindered and restricted water diffusion in brain white matter. Magnetic Resonance In Medicine. 2004; 52:965–978. [PubMed: 15508168]

Bar-Shir A, Cohen Y. High b-value q-space diffusion MRS of nerves: structural information and comparison with histological evidence. NMR in Biomedicine. 2008; 21:165–174. [PubMed: 17492659]

Barazany D, Basser PJ, Assaf Y. In vivo measurement of axon diameter distribution in the corpus callosum of rat brain. Brain. 2009; 132:1210–1220. [PubMed: 19403788]

Baron CA, Beaulieu C. Oscillating gradient spin-echo (OGSE) diffusion tensor imaging of the human brain. Magnetic Resonance in Medicine. 2014; 72:726–736. [PubMed: 24142863]

Basser PJ. Inferring microstructural features and the physiological state of tissues from diffusion-weighted images. NMR in Biomedicine. 1995; 8:333–344. [PubMed: 8739270]

Beaulieu C. The basis of anisotropic water diffusion in the nervous system - a technical review. NMR in Biomedicine. 2002; 15:435–455. [PubMed: 12489094]

Beaulieu C, Allen PS. An in vitro evaluation of the effects of local magnetic-susceptibility-induced gradients on anisotropic water diffusion in nerve. Magnetic Resonance in Medicine. 1996; 36:39–44. [PubMed: 8795018]

Behrens TEJ, Woolrich MW, Jenkinson M, Johansen-Berg H, Nunes RG, Clare S, Matthews PM, Brady JM, Smith SM. Characterization and propagation of uncertainty in diffusion-weighted MR imaging. Magn Reson Med. 2003; 50:1077–1088. [PubMed: 14587019]

Bjarnason TA, Vavasour IM, Chia CLL, MacKay AL. Characterization of the NMR behavior of white matter in bovine brain. Magn Reson Med. 2005; 54:1072–1081. [PubMed: 16200557]

Bouchaud JP, Georges A. Anomalous diffusion in disordered media: Statistical mechanisms, models and physical applications. Physics Reports. 1990; 195:127–293.

Budde MB, Frank JA. Neurite beading is sufficient to decrease the apparent diffusion coefficient after ischemic stroke. PNAS. 2010; 107:14472–14477. [PubMed: 20660718]

Burcaw LM, Fieremans E, Novikov DS. Mesoscopic structure of neuronal tracts from time-dependent diffusion. Neuroimage. 2015; 114:18–37. [PubMed: 25837598]

Callaghan PT, Coy A, MacGowan D, Packer KJ, Zelaya FO. Diffraction-like effects in NMR diffusion studies of fluids in porous solids. Nature. 1991; 351:467–469.

Callaghan PT, Stepišnik J. Frequency-domain analysis of spin motion using modulated-gradient NMR. Journal of Magnetic Resonance, Series A. 1995; 117:118–122.

Clark C, Hedehus M, Moseley M. Diffusion time dependence of the apparent diffusion tensor in healthy human brain and white matter disease. Magnetic Resonance In Medicine. 2001; 45:1126–1129. [PubMed: 11378893]

Clark CA, Le Bihan D. Water diffusion compartmentation and anisotropy at high b values in the human brain. Magn Reson Med. 2000; 44:852–859. [PubMed: 11108621]

Debanne D, Campanac E, Bialowas A, Carlier E, Alcaraz G. Axon Physiology. Physiol Rev. 2011; 91:555–602. [PubMed: 21527732]

Does MD, Gore JC. Compartmental study of T1 and T2 in rat brain and trigeminal nerve in vivo. Magnetic Resonance in Medicine. 2002; 47:274–283. [PubMed: 11810670]

Does MD, Parsons EC, Gore JC. Oscillating Gradient Measurements of Water Diffusion in Normal and Globally Ischemic Rat Brain. Magnetic Resonance In Medicine. 2003; 49:206–215. [PubMed: 12541239]

Fieremans E, Novikov DS, Jensen JH, Helpern JA. Monte Carlo study of a two-compartment exchange model of diffusion. NMR in Biomedicine. 2010; 23:711–724. [PubMed: 20882537]

Henkelman RM, Stanisz GJ, Kim JK, Bronskill MJ. Anisotropy Of Nmr Properties Of Tissues. Magn Reson Med. 1994; 32:592–601. [PubMed: 7808260]

Horsfield M, Barker G, Mcdonald W. Self-Diffusion in Cns Tissue by Volume-Selective Proton NMR. Magnetic Resonance In Medicine. 1994; 31:637–644. [PubMed: 8057816]

Innocenti GM, Caminiti R, Aboitiz F. Comments on the paper by Horowitz et al. (2014). Brain Structure and Function. 2015; 220:1789–1790. [PubMed: 25579065]

Jenkinson M, Bannister PR, Brady JM, Smith SM. Improved optimisation for the robust and accurate linear registration and motion correction of brain images. Neuroimage. 2002; 17:825–841. [PubMed: 12377157]

Jenkinson M, Smith S. A global optimisation method for robust affine registration of brain images. Medical Image Analysis. 2001; 5:143–156. [PubMed: 11516708]

Jespersen SN, Kroenke CD, Østergaard L, Ackerman JJH, Yablonskiy DA. Modeling dendrite density from magnetic resonance diffusion measurements. Neuroimage. 2007; 34:1473–1486. [PubMed: 17188901]

Kroenke CD, Ackerman JJH, Yablonskiy DA. On the nature of the NAA diffusion attenuated MR signal in the central nervous system. Magnetic Resonance in Medicine. 2004; 52:1052–1059. [PubMed: 15508157]

Kunz N, Sizonenko SV, Hueppi PS, Gruetter R, van de Looij Y. Investigation of field and diffusion time dependence of the diffusion-weighted signal at ultrahigh magnetic fields. NMR In Biomedicine. 2013; 26:1251–1257. [PubMed: 23533088]

Lancaster JL, Andrews T, Hardies LJ, Dodd S, Fox PT. Three-pool model of white matter. Journal of Magnetic Resonance Imaging. 2003; 17:1–10. [PubMed: 12500269]

Lavdas I, Behan KC, Papadaki A, McRobbie DW, Aboagye EO. A phantom for diffusion-weighted MRI (DW-MRI). Journal of Magnetic Resonance Imaging. 2013; 38:173–179. [PubMed: 23576443]

Lee, H-H.; Burcaw, LM.; Veraart, J.; Fieremans, E.; Novikov, DS. Low-Pass Filter Effect of Finite Gradient Duration on Time-Dependent Diffusion in the Human Brain. ISMRM 23rd Annual Meeting and Exhibition; 2015; Toronto, Canada. 2015. p. 2777

Lundell H, Alexander DC, Dyrby TB. High angular resolution diffusion imaging with stimulated echoes: compensation and correction in experiment design and analysis. NMR in Biomedicine. 2014; 27:918–925. [PubMed: 24890716]

Merboldt KD, Hanicke W, Frahm J. Self-diffusion NMR imaging using stimulated echoes. Journal of Magnetic Resonance (1969). 1985; 64:479–486.

Mitra PP, Sen PN, Schwartz LM, Le Doussal P. Diffusion Propagator as a Probe of the Structure of Porous Media. Physical Review Letters. 1992; 68:3555–3558. [PubMed: 10045734]

Mori, S. MRI Atlas of Human White Matter. Elsevier; Amsterdam, The Netherlands: 2005.

Mulkern RV, Zengingonul HP, Robertson RL, Bogner P, Zou KH, Gudbjartsson H, Guttmann CR, Holtzman D, Kyriakos W, Jolesz FA, Maier SE. Multi-component apparent diffusion coefficients in human brain: relationship to spin-lattice relaxation. Magn Reson Med. 2000; 44:292–300. [PubMed: 10918329]

Murday JS, Cotts RM. Self-Diffusion Coefficient of Liquid Lithium. The Journal of Chemical Physics. 1968; 48:4938–4945.

Neuman CH. Spin echo of spins diffusing in a bounded medium. The Journal of Chemical Physics. 1974; 60:4508–4511.

Nilsson M, Latt J, Nordh E, Wirestam R, Stahlberg F, Brockstedt S. On the effects of a varied diffusion time in vivo: is the diffusion in white matter restricted? Magnetic Resonance Imaging. 2009; 27:176–187. [PubMed: 18657924]

Nilsson M, Lätt J, Ståhlberg F, van Westen D, Hagslätt H. The importance of axonal undulation in diffusion MR measurements: a Monte Carlo simulation study. NMR in Biomedicine. 2012; 25:795–805. [PubMed: 22020832]

Novikov DS, Jensen JH, Helpern JA, Fieremans E. Revealing mesoscopic structural universality with diffusion. Proceedings of the National Academy of Sciences of the United States of America. 2014; 111:5088–5093. [PubMed: 24706873]

Ong HH, Wright AC, Wehrli SL, Souza A, Schwartz ED, Hwang SN, Wehrli FW. Indirect measurement of regional axon diameter in excised mouse spinal cord with q-space imaging: Simulation and experimental studies. Neuroimage. 2008; 40:1619–1632. [PubMed: 18342541]

Perge JA, Koch K, Miller R, Sterling P, Balasubramanian V. How the Optic Nerve Allocates Space, Energy Capacity, and Information. The Journal of Neuroscience. 2009; 29:7917–7928. [PubMed: 19535603]

Perrot R, Lonchampt P, Peterson AC, Eyer J. Axonal neurofilaments control multiple fiber properties but do not influence structure or spacing of nodes of Ranvier. Journal of Neuroscience. 2007; 27:9573–9584. [PubMed: 17804618]

Rioux JA, Levesque IR, Rutt BK. Biexponential longitudinal relaxation in white matter: Characterization and impact on T1 mapping with IR-FSE and MP2RAGE. Magnetic Resonance in Medicine. 2015 n/a-n/a.

Ronen I, Budde M, Ercan E, Annese J, Techawiboonwong A, Webb A. Microstructural organization of axons in the human corpus callosum quantified by diffusion-weighted magnetic resonance spectroscopy of N-acetylaspartate and postmortem histology. Brain Structure and Function. 2014; 219:1773–1785. [PubMed: 23794120]

Salvador R, Peña A, Menon DK, Carpenter TA, Pickard JD, Bullmore ET. Formal characterization and extension of the linearized diffusion tensor model. Human Brain Mapping. 2005; 24:144–155. [PubMed: 15468122]

Schain AJ, Hill RA, Grutzendler J. Label-free in vivo imaging of myelinated axons in health and disease with spectral confocal reflectance microscopy. Nat Med. 2014; 20:443–449. [PubMed: 24681598]

Shemesh N, Cohen Y. Microscopic and compartment shape anisotropies in gray and white matter revealed by angular bipolar double-PFG MR. Magnetic Resonance in Medicine. 2011; 65:1216–1227. [PubMed: 21305595]

Shepherd G, Raastad M. Axonal varicosity distributions along parallel fibers: a new angle on a cerebellar circuit. The Cerebellum. 2003; 2:110–113. [PubMed: 12880178]

Shepherd GMG, Raastad M, Andersen P. General and variable features of varicosity spacing along unmyelinated axons in the hippocampus and cerebellum. PNAS. 2002; 99:6340–6345. [PubMed: 11972022]

Sigmund EE, Sui D, Ukpebor O, Baete S, Fieremans E, Babb JS, Mechlin M, Liu K, Kwon J, Mcgorty K, Hodnett PA, Bencardino J. Stimulated Echo Diffusion Tensor Imaging and SPAIR T-2-Weighted Imaging in Chronic Exertional Compartment Syndrome of the Lower Leg Muscles. J Magn Reson Imaging. 2013; 38:1073–1082. [PubMed: 23440764]

Stanisz GJ. Diffusion MR in Biological Systems: Tissue Compartments and Exchange. Israel Journal of Chemistry. 2003; 43:33–44.

Stanisz GJ, Kecojevic A, Bronskill MJ, Henkelman RM. Characterizing white matter with magnetization transfer and T2. Magnetic Resonance in Medicine. 1999; 42:1128–1136. [PubMed: 10571935]

Stanisz GJ, Odrobina EE, Pun J, Escaravage M, Graham SJ, Bronskill MJ, Henkelman RM. T1, T2 relaxation and magnetization transfer in tissue at 3T. Magn Reson Med. 2005; 54:507–512. [PubMed: 16086319]

Stanisz GJ, Szafer A, Wright GA, Henkelman RM. An Analyitical Model of Restricted Diffusion in Bovine Optic Nerve. Magnetic Resonance In Medicine. 1997; 37:103–111. [PubMed: 8978638]

Stepišnik J. Time-dependent self-diffusion by NMR spin-echo. Physica B. 1993; 183:343–350.

Szafer A, Zhong J, Gore JC. Theoretical model for water diffusion in tissues. Magnetic Resonance in Medicine. 1995; 33:697–712. [PubMed: 7596275]

Tang Y, Nyengaard JR. A stereological method for estimating the total length and size of myelin fibers in human brain white matter. J Neurosci Methods. 1997; 73:193–200. [PubMed: 9196291]

Tanner JE. Use of the Stimulated Echo in NMR Diffusion Studies. The Journal of Chemical Physics. 1970; 52:2523–2526.

van Gelderen P, Devleeschouwer M, Despres D, Pekar J, Vanzijl P, Moonen C. Water Diffusion And Acute Stroke. Magnetic Resonance in Medicine. 1994; 31:154–163. [PubMed: 8133751]

Veraart J, Fieremans E, Jelescu IO, Knoll F, Novikov DS. Gibss Ringing in Diffusion MRI. Magnetic Resonance in Medicine. 2015 In press.

Veraart J, Sijbers J, Sunaert S, Leemans A, Jeurissen B. Weighted linear least squares estimation of diffusion MRI parameters: Strengths, limitations, and pitfalls. Neuroimage. 2013; 81:335–346. [PubMed: 23684865]

Wang L, Dong J, Cull G, Fortune B, Cioffi GA. Varicosities of Intraretinal Ganglion Cell Axons in Human and Nonhuman Primates. Investigative Ophthalmology and Visual Science. 2003; 44:2–9. [PubMed: 12506048]

Whittall KP, MacKay AL, Graeb DA, Nugent RA, Li DK, Paty DW. In vivo measurement of T2 distributions and water contents in normal human brain. Magn Reson Med. 1997; 37:34–43. [PubMed: 8978630]

Xu J, Li H, Harkins KD, Jiang X, Xie J, Kang H, Does MD, Gore JC. Mapping mean axon diameter and axonal volume fraction by MRI using temporal diffusion spectroscopy. Neuroimage. 2014; 103:10–19. [PubMed: 25225002]

Zhang H, Hubbard PL, Parker GJM, Alexander DC. Axon diameter mapping in the presence of orientation dispersion with diffusion MRI. Neuroimage. 2011; 56:1301–1315. [PubMed: 21316474]

Zhang Y, Brady M, Smith S. Segmentation of brain MR images through a hidden Markov random field model and the expectation-maximization algorithm. IEEE Transactions on Medical Imaging. 2001; 20:45–57. [PubMed: 11293691]

Appendix A Estimating the Disorder Correlation Length from D||(t)

As we increase diffusion time, the diffusion coefficient reflects an effective coarse-graining of the mesoscopic structure over increasing diffusion length. This will result in a reduction of the spatially varying coarse-grained diffusivity component, $\delta D(\mathbf{r}) = D(\mathbf{r}) - D_\infty$. In dimension $d = 1$, the effect of this residual spatial variance on the time dependent diffusion along the fibers can be calculated via the Fourier transform $\Gamma_D(k) = \int \exp(-i\mathbf{k}x)\, \Gamma_D(x)\, dx$ of the two point-correlation function, $\Gamma_D(k) = \langle \delta D(x_0 + x)\delta D(x_0)\rangle$. Defining the instantaneous diffusion coefficient as $D_{\mathrm{inst}} \equiv \frac{\partial}{\partial t}\frac{\langle \delta x^2\rangle}{2}$, where $\delta x = x(t) - x(0)$, the temporally varying contribution $\delta D_{\mathrm{inst}} = D_{\mathrm{inst}}(t) - D_\infty$ to the instantaneous diffusion coefficient (Novikov et al., 2014) is given by

$$\delta D_{\mathrm{inst}}(t) \simeq \frac{\Gamma_D(0)}{D_\infty}\int \exp(-D_\infty k^2 t)\frac{dk}{2\pi} = \frac{\Gamma_D(k \to 0)}{D_\infty}\frac{1}{\sqrt{4\pi D_\infty t}}. \quad \text{(A1)}$$

(Note that the relevant limit $\Gamma_D(k \to 0)$ is not equal to the value $\Gamma_D(k = 0)$ which is physically unimportant, see Appendix B of (Burcaw et al., 2015)). Thus, $D_{\mathrm{inst}}(t)$ is given by

$$D_{\mathrm{inst}} \simeq D_\infty + \frac{\Gamma_D(k \to 0)}{D_\infty}\frac{1}{\sqrt{4\pi D_\infty t}}. \quad \text{(A2)}$$

The instantaneous diffusion coefficient is related to the MRI measured diffusion coefficient, $D(t)$, via $D(t) = \frac{1}{t}\int_0^t D_{\mathrm{inst}}(t')\, dt'$, which when combined with Equation (B2) will yield

$$D(t) \simeq D_\infty + \frac{c_2}{\sqrt{t}}, \qquad c_2 = \frac{\Gamma_D(k \to 0)}{D_\infty}\frac{1}{\sqrt{\pi D_\infty}}. \quad \text{(A3)}$$

We can hence determine the limit $\Gamma_D(k \to 0)$ from the measured D_∞ and c_2 as

$$\Gamma_D(k \to 0) = c_2 \cdot \sqrt{\pi} \cdot D_\infty^{3/2} \quad \text{(A4)}$$

with the units of $\mu m^5/ms^2$. We can then roughly estimate the limit $\Gamma_D(k \to 0)$ of the power spectrum $\Gamma_D(k)$ for the Poissonian disorder as $\Gamma_D(k \to 0) \sim D_\infty^2 l_c^\parallel$ based on the fact that in the real space, $\Gamma_D(x) \simeq \langle [\delta D]^2\rangle\, \delta(x)$ has a sharp peak with amplitude given by the sample variance $\langle [\delta D]^2\rangle \equiv \langle [\delta D(x)]^2\rangle$, and that this variance $\langle [\delta D]^2\rangle \sim D_\infty^2$ because typical

fluctuations of the local coarse-grained diffusivity $\delta D(x)$ cannot be too different from the long time limit D_∞. Hence, we can estimate $l_c^\parallel$ as

$$l_c^\parallel \sim \frac{\Gamma_D(0)}{D_\infty^2} = c_2 \sqrt{\frac{\pi}{D_\infty}} \quad \text{(A5)}$$

that has the desired units of μm, cf. Equation (5) of the main text.

It may seem unexpected that one can determine a length scale, the correlation length $l_c^\parallel$, from the scale-invariant power-law behavior (B3). Fortunately, the prefactor c_2 of the inverse power law behavior (B3) contains the information about $l_c^\parallel$. To gain more intuition about how this length scale enters c_2, we can rewrite the time-dependent part of $D(t)$ as

$$D(t) - D_\infty \sim D_\infty \cdot \frac{l_c^\parallel}{\sqrt{D_\infty t}}. \quad \text{(A6)}$$

Equation (B6) reflects the effect of a gradual coarse-graining of the medium over increasing diffusion $\text{length} \sim \sqrt{D_\infty t}$ when $\sqrt{D_\infty t} \gg l_c^\parallel$, and is asymptotically valid when the relative deviation $[D(t) - D_\infty]/D_\infty$ is small. At shorter times, i.e. times of the order of diffusion time $t_c \sim l_c^{\parallel 2}/D_\infty$ across the correlation length, the power-law behavior (B6) breaks down and crosses over to the short-time limit, where $D(t)$ is close to the free diffusivity D_0. The cross-over time scale t_c between the two regimes would give the most reliable way to determine the correlation length; however, diffusion times of the order of a few ms are very difficult to access directly using clinical gradients. Quantifying the amplitude of the power-law tail (B3) seems to be the only available method to estimate the correlation length without employing either high q values or very short diffusion times, and it is what makes our approach different from earlier studies. Luckily, the correlation length of the relevant restrictions, of a few micrometers, is not much smaller than the diffusion lengths probed in our study, so the tail (B6) of about 10–20% is not too small and can still be experimentally observed; had these restrictions been sub-micrometer, given the experimental noise, we would have only seen the constant tortuosity limit of $D(t)$.

Appendix B The Effect of Orientational Dispersion on D⊥(t)

Consider the geometry of Figure 7. Let us assume axial symmetry in the fiber orientational distribution, as well as axial symmetry of the diffusion tensor

$$\mathbf{\Lambda} = \begin{bmatrix} \lambda_\perp & 0 & 0 \\ 0 & \lambda_\perp & 0 \\ 0 & 0 & \lambda_\parallel \end{bmatrix} \quad \text{(B1)}$$

for each elementary fiber segment in its natural basis. Each elementary fiber segment, defined by the polar and azimuthal angles θ and φ with respect to the fiber tract axis,

contributes $\delta\mathbf{D} = \mathbf{R}\Lambda\mathbf{R}^{-1}$ to the overall diffusion tensor $\mathbf{D}$. The rotation matrix $\mathbf{R}$ is a combination of the tilt via the polar angle and the rotation by the azimuthal angle,

$$\mathbf{R}=\mathbf{R}_z(\phi)\mathbf{R}_y(\theta)= \begin{bmatrix} \cos\phi & \sin\phi & 0 \\ -\sin\phi & \cos\phi & 0 \\ 0 & 0 & 1 \end{bmatrix} \begin{bmatrix} \cos\theta & 0 & \sin\theta \\ 0 & 1 & 0 \\ -\sin\theta & 0 & \cos\theta \end{bmatrix}$$
$$= \begin{bmatrix} \cos\phi\sin\theta & \sin\phi & \cos\phi\sin\theta \\ -\sin\phi\cos\theta & \cos\phi & -\sin\phi\sin\theta \\ -\sin\theta & 0 & \cos\theta \end{bmatrix}. \tag{B2}$$

Summing up the elementary contributions $\delta\mathbf{D}$ from all segments in order to obtain the overall diffusion tensor $\mathbf{D}$ involves averaging over the azimuthal angle φ. Under the symmetry assumption of all φ being equally probable, the resulting tensor $\mathbf{D}$ becomes diagonal in the fiber tract basis, as expected. This gives us the relations between its eigenvalues $D_\perp$ and $D_\parallel$, and the segments' eigenvalues $\lambda_\perp$ and $\lambda_\parallel$ for any θ,

$$\begin{cases} \lambda_\parallel = D_\parallel + \frac{\langle\sin^2\theta\rangle\Delta D}{1-\frac{3}{2}\langle\sin^2\theta\rangle}, \\ \lambda_\perp = D_\perp - \frac{\frac{\langle\sin^2\theta\rangle}{2}\Delta D}{1-\frac{3}{2}\langle\sin^2\theta\rangle}, \end{cases} \qquad \Delta D = D_\parallel - D_\perp. \tag{B3}$$

Applying Equation (B3) to the WM ROIs and the FA thresholded data averaged over all subjects, and finding θ, which corresponds to $\arcsin\sqrt{\langle\sin^2\theta\rangle}$, such that $\lambda_\perp$ becomes independent of t, results in the azimuthal angle values θ shown in Table B1. An example of the resultant $\lambda_\perp$ over a range of θ is shown in Figure B1.

From the figure, it can be seen that the values of θ required to eliminate the radial time-dependence are much greater than that reported in the literature for axon dispersion for all WM and FA thresholded ROIs. Therefore, we conclude that the time-dependence observed in $D_\perp(t)$ is not (solely) due to fiber orientation dispersion in the principal eigenvector.

Table B1

The rotation angle required to eliminate the radial time-dependence. Both WM ROI and FA thresholded data used is averaged over all subjects.

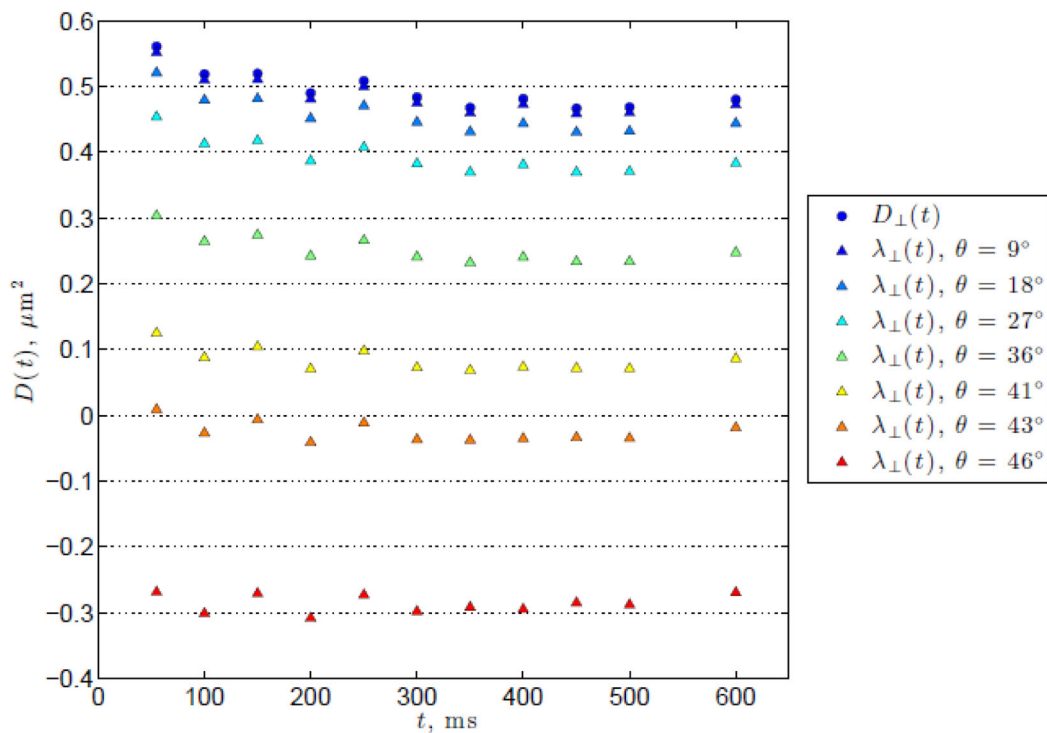| WM ROI	θ	FA Floor	θ
Genu	28°	0.3	49°
Splenium	23°	0.4	46°
ACR	46°	0.5	41°
SCR	53°	0.6	33°
PCR	50°	0.7	0°
PLIC	49°		

Figure B1.
An example of the calculated $\lambda_\perp$ for various θ for the FA > 0.4 ROI. The original measured $D_\perp(t)$ is shown by the blue circles. Calculated $\lambda_\perp$ for a range of θ are shown by the triangles, with increasing θ indicated by the colors ranging from blue to red. Note that at a moderately large angle of $\theta = 36°$ (green triangles) there is still a relatively marked decrease in $\lambda_\perp$ with respect to t.

Highlights

- We measure time-dependent DTI (55 ms – 600 ms) *in vivo* in human white matter

- Pronounced longitudinal and weaker transverse time-dependent diffusion is observed

- Longitudinal time-dependence is attributed to axonal varicosities

- Transverse time-dependence is attributed to the random axon packing geometry

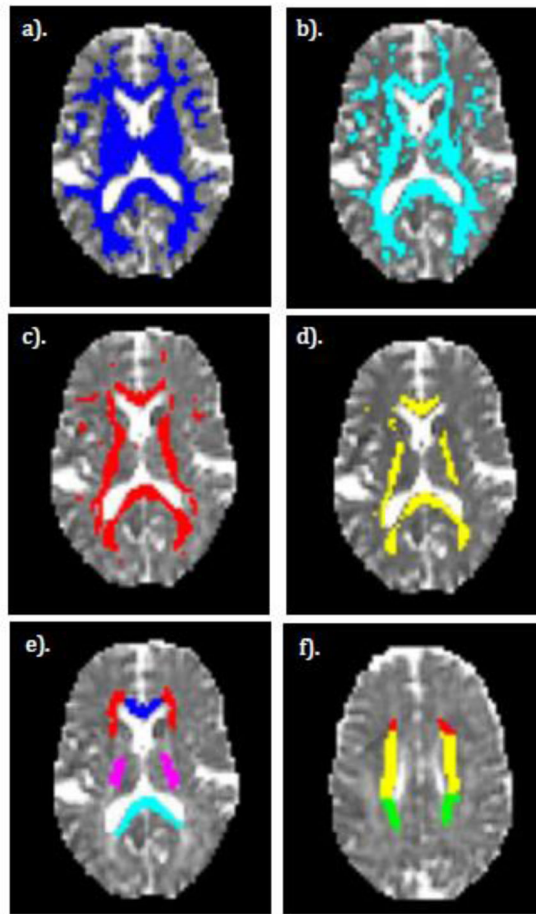- Varying diffusion time may provide a novel microstructural contrast

Figure 1.
Examples of ROIs used in this study displayed on a single subject. a–d). FA thresholded ROIs. e–f). Anatomical WM ROIs. a). FA > 0.3 b). FA > 0.4 c). FA > 0.5 d). FA > 0.6. e). Various anatomical WM ROIs including genu (blue), splenium (cyan), posterior limb of the internal capsule (purple), and the anterior corona radiata (red). f). Same as e), but a more superior slice to show the remaining ROIs including the superior corona radiata (yellow) and the posterior corona radiata (green). The red ROI is a continuation of the anterior corona radiata as seen in e).
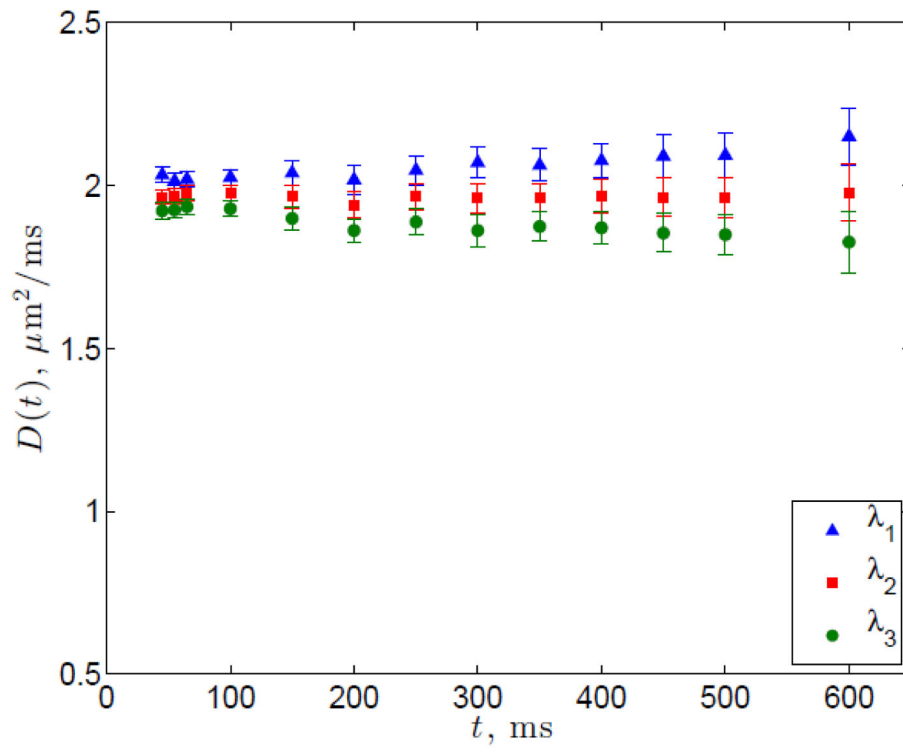
Figure 2.
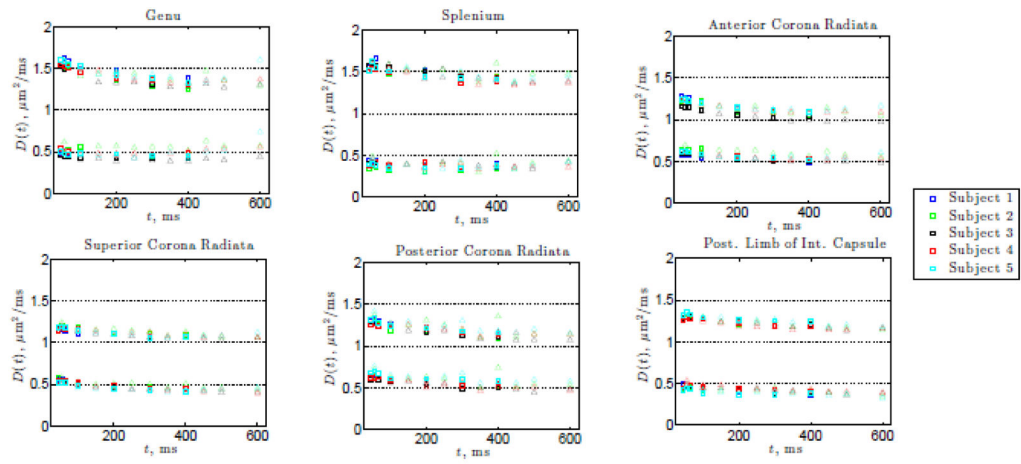Diffusion tensor eigenvalues in the agarose-nickel phantom from scan 1

Figure 3.
The longitudinal and transverse diffusivities, $D_\parallel(t)$ and $D_\perp(t)$, for the 6 WM ROIs as a function of the diffusion time t shown for all subjects. Squares indicate scan 1 data, and triangles denote scan 2.
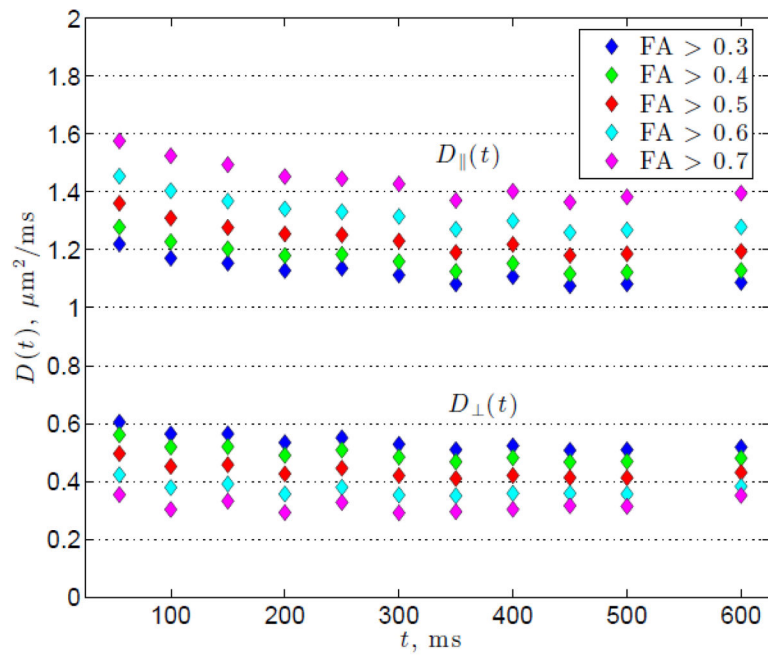
Figure 4.
The longitudinal and transverse diffusivities, $D_\parallel(t)$ and $D_\perp(t)$, averaged over all subjects for each FA thresholded ROI as a function of the diffusion time t.
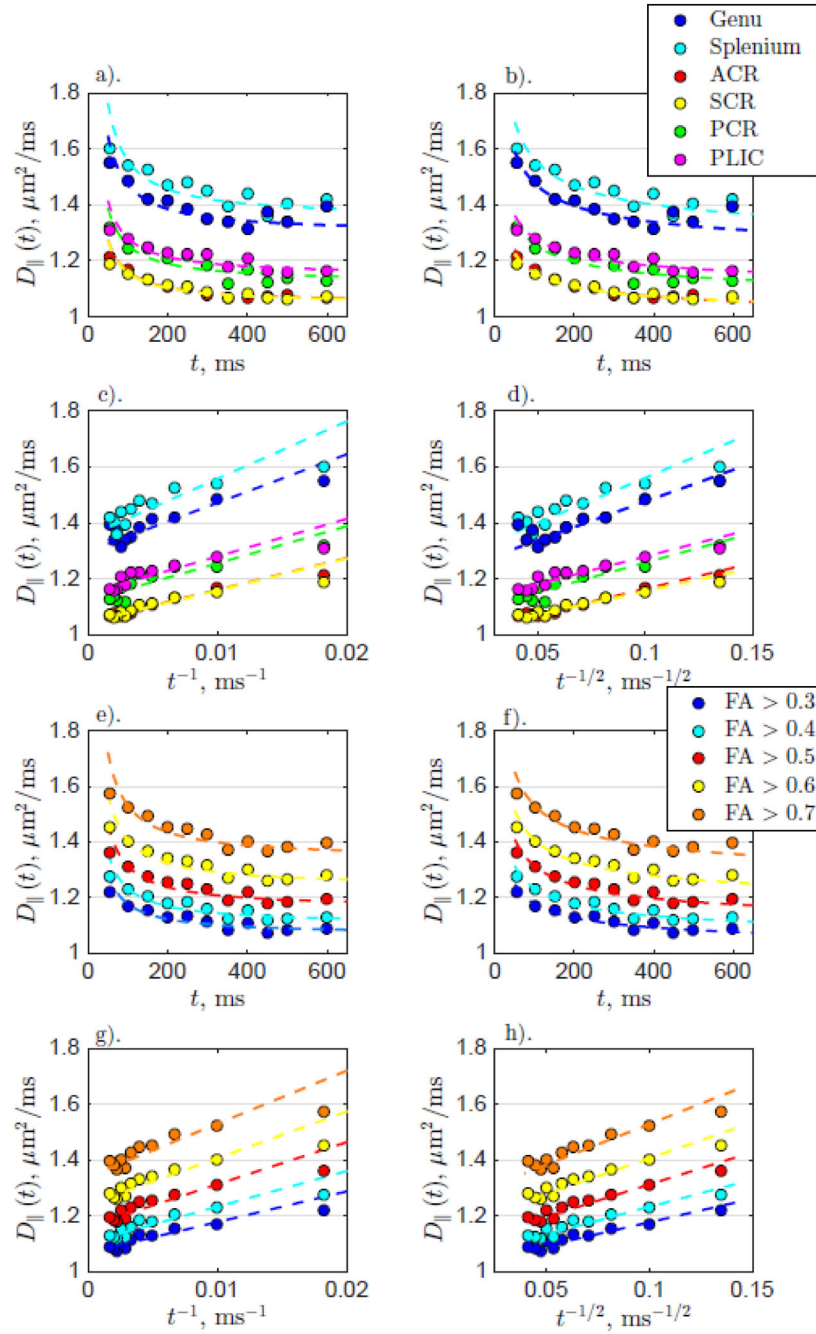
Figure 5.
$D_{\parallel}(t)$ for anatomical WM and FA thresholded ROIs for all subjects. The left column shows the fit for longitudinally ordered restrictions (Equation (3)) and the right column shows the fit for longitudinally disordered restrictions (Equation (4)). The top two and bottom two rows show the data from the anatomical WM ROIs and the FA thresholded ROIs, respectively. a). WM $D_{\parallel}(t)$ fit with time-dependence coming from ordered restrictions (Equation (3)) plotted with respect to t. b). WM $D_{\parallel}(t)$ fit assuming disordered restrictions (Equation (4)) plotted with respect to t. c). The same as for a). but plotted with respect to t^{-1}.

d). The same as for b). but plotted with respect to $t^{-1/2}$. e–h). The same as for a–d). but with FA thresholded ROIs.
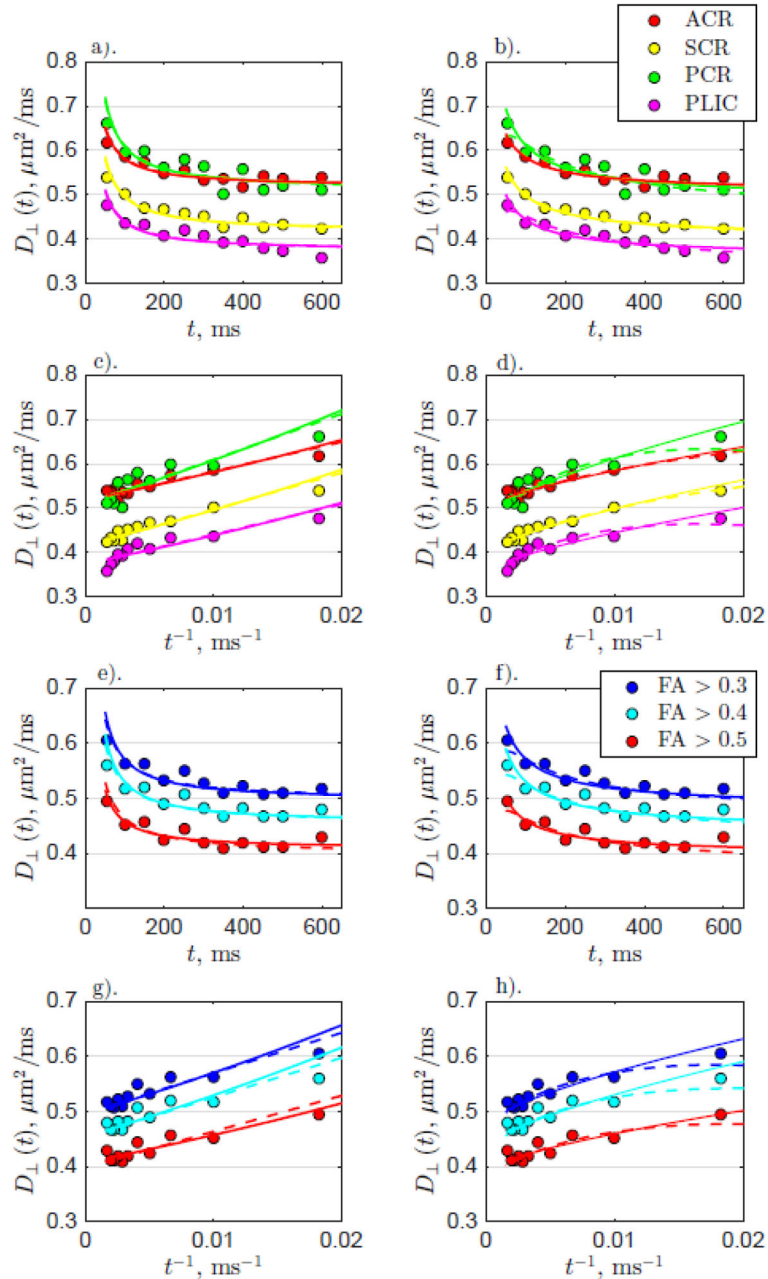
Figure 6.

$D_\perp(t)$ for both anatomical WM and FA thresholded ROIs for all subjects. The left column shows the fits with time-dependence arising from intra-axonal diffusion (Equations (6) and (7)), while the right columns shows the fits with time-dependence arising from extra-axonal diffusion (Equations (8) and (9)). As in Figure 5, the top two and bottom two rows show the data from the WM and FA ROIs, respectively. Similar to the longitudinal diffusivity, data from scans 1 and 2 are averaged over all subjects and shown by the circles. a). Anatomical WM $D_\perp(t)$ fit with time-dependence coming from intra-axonal diffusion (dashed: narrow pulse limit Equation (6); solid: wide pulse limit Equation (7)) plotted with respect to t. b).

Anatomical WM $D_\perp(t)$ fit with time-dependence originating from extra-axonal diffusion within a disordered structure (dashed: narrow pulse limit Equation (8); solid: wide pulse limit Equation (9)) with respect to t. c). The same as for a). but plotted with respect to t^{-1}. d). The same as for b). but plotted with respect to t^{-1}. e–h). The same as for a–d). but FA thresholded ROI data
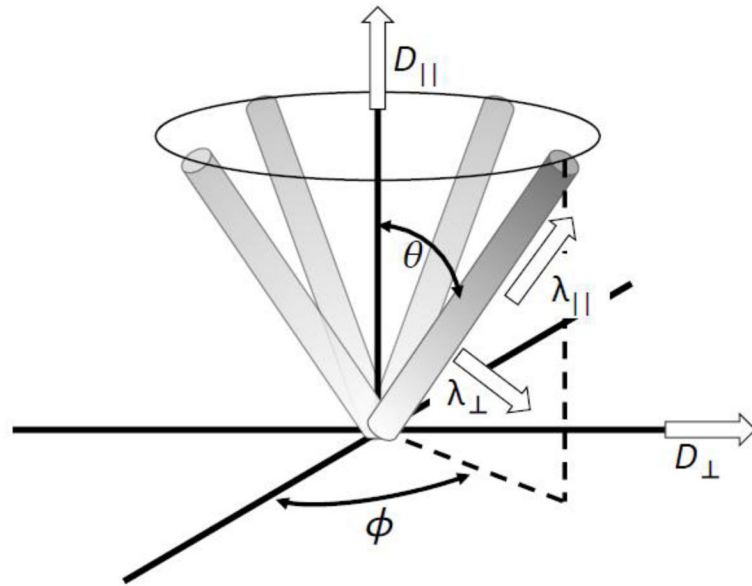
Figure 7.
Schematic illustrating the axially symmetric set of elementary fiber segments with eigenvalues $\lambda_\perp$ and $\lambda_\parallel$ contributing to the overall voxel-wise diffusion tensor eigenvalues $D_\perp$ and $D_\parallel$.

Table 1

Scan parameter summaries.

Scan session	# t points	t, ms	δ, ms	TE, ms	TR, ms
1	6	45–300	20	100	7000
	1	400	20	100	7300
2	7	55–350	20	100	7000
	1	400	20	100	7300
	1	450	20	100	8000
	1	500	20	100	8700
	1	600	20	100	10200

Table 2

ROI fitting parameters for $D_{\parallel}(t)$ assuming longitudinally ordered restrictions (Equation (3)). *P*-values are given after Bonferroni correction (×22). All units are μm and ms.

ROI	Longitudinal Diffusion with Ordered Restrictions (Eq. (3))						Longitudinal Diffusion with Disordered Restrictions (Eq. (4))						
	R^2	P	D_∞	c_1	a	$D_{\parallel}(t)$ % Change	R^2	P	D_∞	c_2	$\Gamma_{\mathrm{D}}(0)$	$l_{\mathrm{c}}^{\parallel}$	$D_{\parallel}(t)$ % Change
Genu	0.849	1.24e-3	1.30	17.39	4.17	−17.8	0.875	5.25e-4	1.20	2.77	6.45	4.48	−18.6
Splenium	0.751	1.22e-2	1.35	20.54	4.53	−19.7	0.829	2.16e-4	1.24	3.22	7.88	5.13	−20.3
ACR	0.926	4.75e-5	1.05	11.35	3.37	−14.9	0.957	4.13e-6	0.98	1.84	3.17	3.30	−15.9
SCR	0.875	5.13e-4	1.05	11.4	3.38	−14.9	0.905	1.50e-4	0.99	1.67	2.91	2.97	−14.6
PCR	0.708	2.56e-2	1.12	13.3	3.65	−16.1	0.780	6.95e-3	1.05	2.11	4.01	3.66	−16.8
PLIC	0.891	2.73e-4	1.15	13.44	3.67	−15.9	0.935	2.60e-5	1.08	1.97	3.94	3.36	−15.5
FA > 0.3	0.866	7.15e-4	1.07	11.12	3.33	−14.5	0.910	1.18e-4	1.01	1.71	3.05	3.02	−13.0
FA > 0.4	0.888	3.10e-4	1.10	13.10	3.62	−16.2	0.925	5.16e-5	1.03	2.01	3.72	3.50	−14.5
FA > 0.5	0.882	3.92e-4	1.16	15.10	3.89	−17.3	0.921	6.42e-5	1.08	2.32	4.62	3.95	−15.6
FA > 0.6	0.861	8.18e-4	1.24	17.00	4.12	−18.1	0.907	1.39e-4	1.15	2.61	5.68	4.31	−16.3
FA > 0.7	0.793	5.25e-3	1.34	18.02	4.24	−17.8	0.827	2.27e-3	1.25	2.78	6.86	4.42	−16.1

Table 3

ROI fitting parameters for transverse diffusion coefficient $D_\perp(t)$. P-values are given after Bonferroni correction ($\times 22$). Here $D_\infty = f_{ext} D_\infty^{ext}$ is the estimated bulk diffusion coefficient (tortuosity limit) transverse to the axonal tract. In the intra-axonal picture, the columns $2r\sqrt{f_{int}}$ and $2r(f_{int}/D_0)^{1/4}$ set lower bounds on typical axonal diameters $2r$, since $f_{int} < 1$ and $f_{int}/D_0 < 1$. Likewise, in the extra-axonal picture, the column $l_c^\perp \sqrt{f_{ext}}$ sets the lower bound on the fiber packing correlation length. For details, see *Theory* section. All units are μm and ms.

| | | | $D_\perp(t)$ arising from intra-axonal diffusion only: | | | | | | $D_\perp(t)$ from extra-axonal diffusion in a disordered fiber bundle: | | | | | | |
| | | | Narrow pulse (Eq. (6)) | | | Neuman's limit (Eq. (7)) | | | Narrow pulse (Eq. (8)) | | | Finite pulse width (Eq. (9)) | | | |
ROI	$D_\perp(t)$ % change	P	D_∞	$2r\sqrt{f_{int}}$	R^2	D_∞	$2r\left(\frac{f_{int}}{D_0}\right)^{1/4}$	R^2	D_∞	$f_{ext}A$	$\tilde{t_c}$	D_∞	$f_{ext}A$	$l_c^\perp\sqrt{f_{ext}}$	R^2
Genu	-	1.39	-	-	-	-	-	-	-	-	-	-	-	-	-
Splenium	-	0.604	-	-	-	-	-	-	-	-	-	-	-	-	-
ACR	−20.6	4.07e-3	0.52	10.31	0.804	0.52	10.66	0.791	0.50	3.14	6.32	0.50	2.41	3.47	0.822
SCR	−28.4	7.20e-5	0.41	11.49	0.919	0.42	11.28	0.906	0.39	4.06	7.40	0.40	2.93	3.83	0.940
PCR	−28.7	2.56e-2	0.51	12.82	0.708	0.51	11.88	0.689	0.45	10.88	21.38	0.49	3.75	4.33	0.755
PLIC	−26.7	1.18e-2	0.37	10.44	0.753	0.37	10.70	0.733	0.33	8.34	22.36	0.36	2.56	3.58	0.812
FA > 0.3	−20.81	2.42e-3	0.49	11.14	0.825	0.50	11.13	0.812	0.46	7.40	21.29	0.41	2.73	3.69	0.855
FA > 0.4	−21.62	4.07e-3	0.45	11.16	0.804	0.45	11.14	0.789	0.42	7.49	21.91	0.40	2.73	3.69	0.838
FA > 0.5	−17.30	1.39e-2	0.41	9.17	0.744	0.41	10.06	0.734	0.39	2.83	8.26	0.40	1.91	3.09	0.754
FA > 0.6	-	7.88e-2	-	-	-	-	-	-	-	-	-	-	-	-	-
FA > 0.7	-	7.76	-	-	-	-	-	-	-	-	-	-	-	-	-